AGU PUBLICATIONS

JGR

Journal of Geophysical Research: Oceans

RESEARCH ARTICLE

10.1002/2015JC011530

Modeling surfzone to inner-shelf tracer exchange

Kai Hally-Rosendahl[1] and Falk Feddersen[1]

[1]Integrative Oceanography Division, Scripps Institution of Oceanography, UCSD, La Jolla, California, USA

Key Points:
- The Boussinesq model funwaveC accurately simulates surfzone and inner-shelf dye observations and mass balances up to 2 km downstream
- At this alongshore-uniform beach, the surfzone to inner-shelf dye tracer exchange is dominated by transient rip currents
- Inner-shelf vertical variation (dye, velocity, temperature) and tidal changes may cause overpredicted inner-shelf dye mass at long times

Correspondence to:
K. Hally-Rosendahl,
kai@coast.ucsd.edu

Citation:
Hally-Rosendahl, K., and F. Feddersen (2016), Modeling surfzone to inner-shelf tracer exchange, *J. Geophys. Res. Oceans*, *121*, 4007–4025, doi:10.1002/2015JC011530.

Received 5 DEC 2015
Accepted 19 APR 2016
Accepted article online 21 APR 2016
Published online 12 JUN 2016

Abstract A near-shoreline, continuous dye release at an approximately alongshore-uniform beach (IB09 experiment) is simulated with the wave-resolving Boussinesq model funwaveC. The model generates surfzone eddies and transient rip currents but does not resolve inner-shelf vertical variation or stratification. The funwaveC model reproduces well the observed surfzone and inner-shelf dye observations over roughly 350 m cross-shore and 2 km alongshore. Dye is advected alongshore by wave- and wind-driven currents similarly in the observations and model. Near-shoreline mean dye concentration decays downstream as a power law with similar observed (−0.33) and modeled (−0.38) exponents. Observed and modeled cross-shore mean dye profiles are similar, though modeled inner-shelf dye is somewhat elevated. Observed and modeled alongshore dye transports agree, though with compensating surfzone and inner-shelf errors later in the release. For times $<$3.5 h (before observed and modeled dye advects beyond the model alongshore domain), observed and modeled dye budgets are similar to each other and close to within 10%, and half the observed and modeled dye is exported to the inner-shelf. Later in the release, surfzone and inner-shelf dye masses are under and overpredicted, respectively. Model-data differences may be due to the model's lack of vertical variation, stratification, or tide. The good overall model-data agreement indicates that nearshore tracer transport and dispersion are realistically simulated over 5 h and 2 km alongshore, and that the model transient rip currents accurately induce cross-shore exchange between the surfzone and inner-shelf.

1. Introduction

The nearshore region, consisting of the surfzone (shoreline to x_b, the seaward boundary of depth-limited wave breaking) and the inner-shelf (x_b to approximately 20 m water depth), is of vital economic, ecological, and recreational importance. Maintaining the well-being of this region requires understanding the exchange of tracers (e.g., sediment, larvae, nutrients, and pollutants) between the surfzone and inner-shelf, which have dramatically different dynamical regimes. Despite the importance of this region to our economy and health, understanding of nearshore tracer mixing and transport remains relatively poor.

Several field experiments have tracked Lagrangian surface drifters on alongshore-uniform beaches [e.g., *Spydell et al*., 2007, 2009, 2014] and rip-channeled beaches [e.g., *Brown et al*., 2009; *MacMahan et al*., 2010; *Brown et al*., 2015] to explore nearshore transport and dispersion. Similarly, surfzone fluorescent dye release experiments have also been used to investigate tracer mixing and transport [e.g., *Harris et al*., 1963; *Inman et al*., 1971; *Grant et al*., 2005]. However, these observations were limited by sparse sampling. Jetski-based cross-surfzone dye profiles improved sampling and enabled statistical surfzone cross-shore diffusivity estimates [*Clark et al*., 2010]. However, these diffusivities were for alongshore distances generally $\leq$200 m from the dye release and for short times when the dye was surfzone-contained. Until recently, a quantitative coupled surfzone and inner-shelf tracer mass budget had never been performed, and dye tracer mass balance closure has remained elusive in larger-scale oceanographic contexts [e.g., *Tulloch et al*., 2014].

By combining a suite of dye, wave, and velocity observations from a dye release at an approximately alongshore-uniform beach (IB09 experiment), *Hally-Rosendahl et al*. [2015] (hereafter HR15) closed a tracer mass budget and showed that about half of the surfzone-released dye was exported to the inner-shelf over 5 h and 3.2 km downstream. The primary driver of this cross-shore exchange was transient rip currents, which occur due to the coalescing of surfzone eddies generated by finite crest length wave breaking [*Peregrine*, 1998; *Clark et al*., 2012]. However, a coupled surfzone and inner-shelf tracer model-data comparison, particularly over these larger scales, has never been performed.

Wave-resolving models include this surfzone eddy generation mechanism, but wave-averaged models do not [*Feddersen*, 2014]. Wave-resolving models have been used to show that, for mean normally-incident waves, surfzone to inner-shelf transient rip current driven exchange velocities depend strongly on the wave directional spread [*Suanda and Feddersen*, 2015]. However, wave-resolving models are essentially depth-averaged and thus do not include vertical variation or stratification effects. In *Hally-Rosendahl et al*. [2014] (hereafter HR14) and HR15, dye concentration was vertically uniform within the surfzone. However, on the inner-shelf, dye was surface-intensified due to stratification. As the surfzone and inner-shelf have such different dynamics, it is not clear if a depth-averaged wave-resolving model can accurately reproduce the cross-shore exchange between these two regions.

Here, the wave-resolving Boussinesq model funwaveC [e.g., *Spydell and Feddersen*, 2009; *Feddersen et al*., 2011; *Suanda and Feddersen*, 2015] is used to simulate the HR15 dye release. In moderate alongshore currents, the funwaveC model has been shown to accurately reproduce observed cross-shore tracer diffusivity within the surfzone [*Clark et al*., 2011]. However, this study was limited to short cross-shore (generally $\leq$100 m) and alongshore (generally $\leq$200 m) distances from the release when dye was surfzone-contained, and thus the diffusivity estimates were surfzone-specific. Although the dispersion of shoreline-source tracers is initially within the surfzone, tracer fate is ultimately determined by exchange between the surfzone and the inner-shelf [e.g., HR14; HR15], occurring over longer time and larger cross- and alongshore scales than those previously modeled.

Here, we investigate funwaveC's ability to reproduce the coupled surfzone and inner-shelf dye observations and dye mass budget of HR15. The IB09 dye release experiment and the funwaveC model are briefly described in section 2. Qualitative and quantitative comparisons of observed and modeled dye are presented in section 3. A model dye mass budget is performed and compared to the observations of HR15 in section 4. The results are discussed in section 5 and summarized in section 6.

2. Methods: Observations and Model

2.1. IB09 Observations: 13 October

The 13 October 2009 dye release [HR15] as part of the IB09 field experiment at Imperial Beach, CA [e.g., *Feddersen*, 2012a; *Spydell et al*., 2014; *Rippy et al*., 2013] is briefly described here. Full details are in HR15. The shoreline and bathymetry are approximately alongshore-uniform (Figure 1), with cross-shore coordinate $x = 0$ m at the mean shoreline increasing negatively seaward, and alongshore coordinate $y = 0$ m at the dye release location increasing positively toward the north. The vertical coordinate $z = 0$ m at mean sea level and increases positively upward. Fluorescent Rhodamine WT dye was released continuously at Q=512 ppb m^3 s^{-1} near the shoreline at $(x_{rl}, y_{rl}) = (-10, 0)$ m for approximately 6.5 h, with $t = 0$ s defined here as the dye release start time. While dispersing cross-shore, dye was advected alongshore by breaking-wave- and wind-driven currents, forming a several kilometer long, shoreline-attached plume.

Waves, currents, and dye concentration were measured on a 125-m long cross-shore array of six near-bottom frames (denoted f1−f6 onshore to offshore, Figure 1, diamonds) located at $y_f = 248$ m. Near-shoreline dye was measured with four thermistor-equipped ECO Triplet fluorometers (ETs) deployed at $y = 82$, 546, 1069, and 1662 m after the dye release had started. The f2 instruments (at $y_f = 248$ m) are used in conjunction with these four ETs to make the near-shoreline array SA1–SA5 (Figure 1, circles and gray diamond). Frame and SA observations are averaged over 30 s to filter out individual wave effects. Surface dye concentration was measured using two GPS-tracked jetskis [*Clark et al*., 2009] that drove repeated cross-shore transects from $x \approx -400$ m to the shoreline (e.g., Figure 1) at various designated alongshore locations between $y = 5$ m and $y \approx 2$ km [HR15]. Inner-shelf upper water column dye concentration was measured with a vertical array ($z = -1$ to -2.5 m at 0.5 m spacing) of ETs towed alongshore behind a small boat. Repeated $\approx$ 2 km alongshore transects (e.g., Figure 1) were driven at roughly 1 m s^{-1} at a mean cross-shore location nominally two surfzone widths from the shoreline. Near-surface dye concentration was also observed remotely from a small plane using a georeferenced multispectral camera system [*Clark et al*., 2014]. The dye field was imaged from the shoreline to approximately $\approx$ 350 m offshore and from the release to $\approx$ 3.2 km downstream. Quantitative aerial image analyses are confined to the inner-shelf due to surfzone noise from wave breaking foam [HR15].

2.2. Wave-Resolving funwaveC Model

2.2.1. Model Waves and Currents

A description of the wave-resolving, Boussinesq funwaveC model is provided here, and additional details can be found elsewhere [*Spydell and Feddersen*, 2009; *Feddersen et al.*, 2011; *Suanda et al.*, 2016]. The funwaveC model equations [*Nwogu*, 1993] are similar to the nonlinear shallow water equations but allow for higher-order dispersion. The mass conservation equation is

$$\frac{\partial \eta}{\partial t} + \nabla \cdot [(h+\eta)\boldsymbol{u}] + \nabla \cdot \boldsymbol{M}_d = 0, \tag{1}$$

where η is the instantaneous free surface elevation, t is time, h is the still water depth, $\boldsymbol{u}$ is the instantaneous horizontal velocity vector at the reference depth $z_r = -0.531h$ (with $z = 0$ m at the still water surface), and $\boldsymbol{M}_d$ is a dispersive term [*Nwogu*, 1993]. The horizontal gradient operator ∇ acts on the cross-shore (x) and alongshore (y) directions. The momentum equation is

$$\frac{\partial \boldsymbol{u}}{\partial t} + \boldsymbol{u} \cdot \nabla \boldsymbol{u} = -g\nabla\eta + \mathbf{F}_d + \mathbf{F}_{\mathrm{br}} - \frac{\tau_b}{(h+\eta)} + \frac{\tau_w}{(h+\eta)} - \nu_{\mathrm{bi}}\nabla^4\boldsymbol{u}, \tag{2}$$

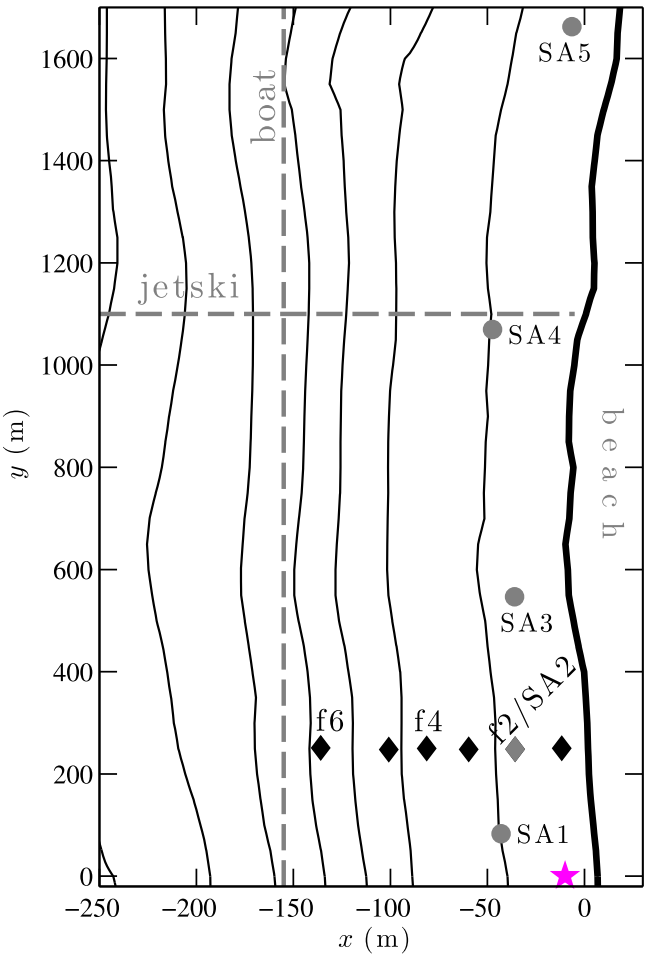

Figure 1. Planview of Imperial Beach bathymetry contours versus cross-shore coordinate x and alongshore coordinate y. Star indicates the 13 October 2009 dye release location. Diamonds denote the cross-shore array of bottom-mounted instrument frames f1-f6 (onshore to offshore). Circles and gray diamond indicate the near-shoreline array SA1–SA5. Vertical-dashed line represents an idealized boat alongshore transect driven repeatedly near this cross-shore location. Horizontal-dashed line represents an idealized jetski cross-shore surface transect driven repeatedly at various alongshore locations.

where g is gravity and $\mathbf{F}_d$ is a dispersive term [*Nwogu*, 1993]. The breaking term $\mathbf{F}_{\mathrm{br}}$ is parameterized as a Newtonian damping [*Kennedy et al.*, 2000; *Lynett*, 2006] with standard parameters [e.g., *Guza and Feddersen*, 2012]. The instantaneous bottom stress τ_b is given by a quadratic drag law,

$$\tau_b = c_d|\boldsymbol{u}|\boldsymbol{u}, \tag{3}$$

with nondimensional drag coefficient $c_d = 2.25\times10^{-3}$, consistent with previous momentum balances and Boussinesq modeling studies [e.g., *Feddersen et al.*, 1998; *Chen et al.*, 2003; *Feddersen and Guza*, 2003; *Feddersen*, 2012b; *Feddersen et al.*, 2011; *Feddersen*, 2014]. The applied wind stress τ_w is alongshore (+ y) at 8.5×10^{-5} m^2 s^{-2}, consistent with the observed southerly mean wind [HR15]. The biharmonic friction ($\nabla^4\boldsymbol{u}$) term damps instabilities with hyperviscosity $\nu_{\mathrm{bi}} = 0.5$ m^4 s^{-1}.

The alongshore-uniform model bathymetry is an alongshore average of the observed approximately alongshore-uniform bathymetry at Imperial Beach, with an added offshore $\approx$ 300 m region of constant 7 m depth and a planar subaerial beach (slope $\beta = 0.02$) extending 2 m above mean sea level to allow runup (Figure 2). In the constant 7 m depth region, there is a wavemaker [*Wei et al.*, 1999] and a 100 m offshore sponge layer to absorb seaward propagating waves. Shoreline runup utilizes the thin layer method [*Salmon*, 2002] as described in *Guza and Feddersen* [2012].

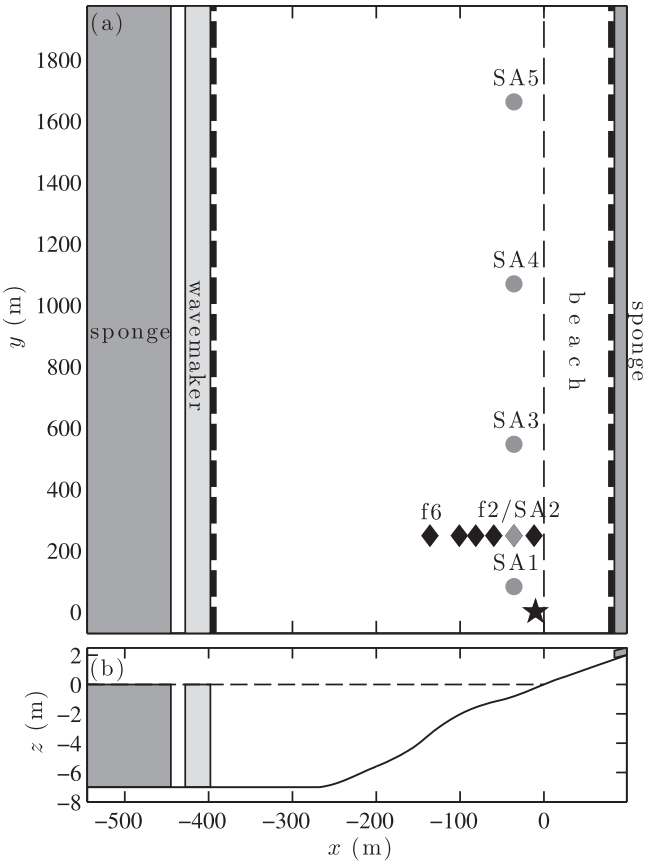

Figure 2. (a) Planview of funwaveC model domain. Cross-shore coordinate x is the distance from the mean shoreline ($x = 0$ m, thin-dashed line). Alongshore coordinate y is the distance from the dye release location ($y = 0$ m, star). Dark gray regions indicate offshore and onshore sponge layers. Light gray region indicates the wavemaker. The cross-shore tracer domain (heavy-dashed lines) is bounded by the wavemaker and the onshore sponge layer. Diamonds denote the cross-shore array of frames f1-f6 (onshore to offshore). Circles and gray diamond indicate the near-shoreline array SA1–SA5. (b) Alongshore-uniform model bathymetry h (curve) versus x with a constant 7 m depth region for the wavemaker and offshore sponge layer, and a planar ($\beta = 0.02$) subaerial beach for runup.

A small sponge layer at the shoreward boundary of the beach face absorbs any runup wave energy that reaches this location. The model cross-shore and alongshore grid sizes are 1 m and 1.35 m, respectively. The total cross-shore domain width is 650 m, and the alongshore domain is 2025 m with alongshore-periodic boundary conditions for η and $\boldsymbol{u}$. The model coordinate system is fixed and is the same as in the observations (section 2.1). The wavemaker, forced at 801 random frequencies [*Suanda et al.*, 2016] spanning $0.04 < f < 0.25$ Hz, approximately generates the back-refracted, release-averaged wave field observed at f6 (Figure 1). The realistic, directionally spread, modeled incident wave field enables surfzone vorticity to be generated at the small length scales of individual short-crested breaking waves [e.g., *Peregrine*, 1998; Clark et al., 2012] and at the larger length scales of wave groups. The model time step is 6.25×10^{-3} s. Instantaneous sea surface elevation η, cross-shore (u), and alongshore (v) velocities are output every 2 s over the entire spatial domain and every 1 s for select linear transects. The simulation was run for 36,000 s, and model output is analyzed after 3000 s, once mean-square vorticity has equilibrated [e.g., *Feddersen et al.*, 2011].

2.2.2. Model Tracer

The funwaveC tracer module is used to simulate the observed 13 October dye release [HR15]. The model dye tracer D_m evolves according to a depth-integrated advection-diffusion equation [*Clark et al.*, 2011],

$$\frac{\partial[(h+\eta)D_m]}{\partial t} + \nabla \cdot [(h+\eta)\boldsymbol{u}D_m] = \nabla \cdot [(\kappa_{br}+\kappa_0)(h+\eta)\nabla D_m] + Q\delta(x-x_{rl})\delta(y-y_{rl}), \quad (4)$$

where the breaking wave eddy diffusivity κ_{br} is nonzero only on the face of breaking waves and is set equal to the breaking wave eddy viscosity ν_{br} (i.e., the tracer Schmidt number is unity). A small background diffusivity $\kappa_0 = 0.075\ \mathrm{m^2\ s^{-1}}$ (applied everywhere, required to ensure non-negative $D_{m)}$ is an order of magnitude smaller than bulk surfzone cross-shore tracer diffusivities observed by *Clark et al.* [2010] for conditions similar to 13 October at IB09. Model dye is released at the same rate $Q = 512\ \mathrm{ppb\ m^3\ s^{-1}}$ and the same location $(x_{rl}, y_{rl}) = (-10, 0)$ m as in the observations (section 2.1), and δ is the Kronecker delta function.

The tracer module cross-shore domain (heavy-dashed lines, Figure 2a) is contained within the larger funwaveC domain (section 2.2.1). A no-flux tracer boundary condition is applied at the top of the beach, and the offshore tracer boundary condition zeros out D_m just onshore of the wavemaker. In contrast to the periodic alongshore boundary conditions for η and $\boldsymbol{u}$, the D_m alongshore boundaries are open at both ends, which allows D_m to advect out of the model domain but not recirculate back in. Model dye is released 67.5 m away from the southern boundary (Figure 2a, star). The tracer module is turned on after 3000 s of simulation

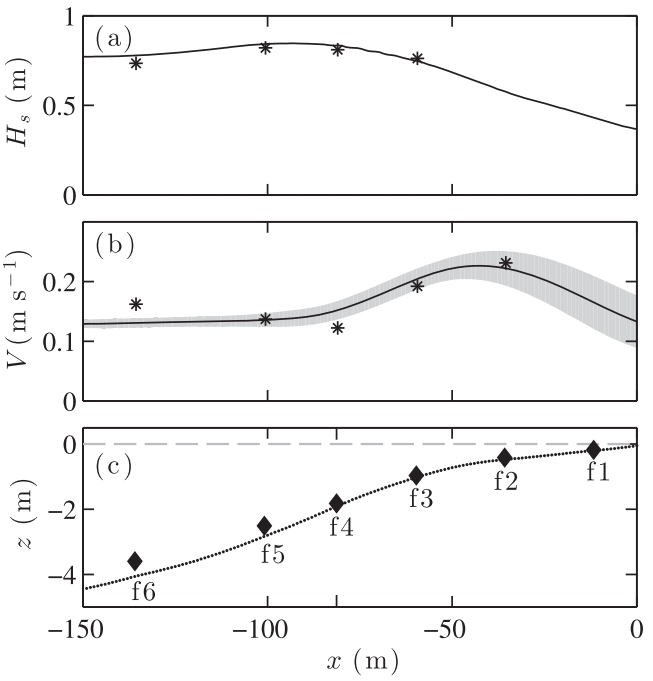

Figure 3. Observed (symbols) and modeled (curves) time-averaged (a) significant wave height H_s and (b) alongshore current V (with modeled alongshore standard deviation shaded) versus cross-shore coordinate x. (c) Locations of f1-f6, with the black curve giving the bathymetry $h(x)$.

once mean square vorticity has equilibrated. Instantaneous D_m snapshots are output every 2 s over the entire spatial domain and averaged over 30 s to filter out individual wave effects as with the observations. In both the model and the observations, $t = 0$ s is the dye release start time.

3. Model-Data Comparisons

Model-data comparisons are analyzed first for waves and currents, and then for various tracer quantities. Throughout, observed quantities are denoted with the $(\,)_o$ subscript, and modeled quantities with $(\,)_m$.

3.1. Waves and Currents

During the 13 October IB09 dye release, the observed wave field is dominated by southerly swell with peak period $T_{p_o} = 13$ s. Averaged over the release, the maximum observed significant wave height $H_{s_o} = 0.87$ m occurs at f4 (Figure 3a, symbols). The modeled wave field, forced with the back-refracted f6-observed spectrum, has maximum $H_{s_m} = 0.89$ m occurring between f5 and f4 (Figure 3a, curve). The model-data H_s root mean square error (rmse) is 0.03 m. As in HR15, the surfzone/inner-shelf boundary $x_b = -81$ m is defined as the cross-shore location of f4 (Figure 3c), where modeled and observed H_s are maximum. The observed mean alongshore current $V_o(x)$ is northward at all frames with a surfzone maximum of 0.23 m s^{-1} (Figure 3b, symbols). Observed $V_o(x)$ decreases to a 0.12 m s^{-1} minimum near the seaward surfzone boundary, and then increases slightly offshore due to the alongshore wind forcing. Modeled $V_m(x)$ has a similar profile with a 0.22 m s^{-1} maximum (Figure 3b, curve). Without wind forcing in the model, the inner-shelf V_m would be near-zero, and the resulting model-data comparison would be poor. The model-data rmse for V is 0.02 m s^{-1}, and model-data agreement is particularly good for the surfzone where the alongshore currents are strongest.

3.2. Surfzone and Inner-Shelf Dye Evolution

The 13 October near-surface dye field was aerially observed over nearly 5 h after the start of the dye release (Figure 4) and described in detail by HR15. Here, for convenience, time is given as hh:mm after the start of the release. All subsequent analyses are in seconds after the start of dye release. The observed dye maps are cross-shore-partitioned into the surfzone (SZ) and inner-shelf (IS) regions (separated by $x_b = -81$ m, section 3.1) and alongshore-partitioned into near and far-field regions A and B (separated by the cross-shore frame array at $y_f = 248$ m, Figure 4a). Note that due to wave-breaking foam, the aerial observations are not able to consistently resolve surfzone dye (regions blacked out in Figure 4); aerial image quantitative analyses are therefore restricted to the inner-shelf.

The aerial images (Figure 4) show the observed surfzone dye advecting alongshore at ≈ 0.25 m s^{-1}, consistent with in situ velocity observations (Figure 3b). While advecting downstream, surfzone dye is ejected offshore to the inner-shelf in alongshore-narrow (≈ 50 m) transient rip currents (Figure 4). Inner-shelf dye features advect downstream at ≈ 0.15 m s^{-1}, slower than the surfzone advection and consistent with in situ f5 and f6 V_o observations (Figure 3b). At $y > 1000$ m, inner-shelf dye has both spread further offshore and dispersed more alongshore than near the release (e.g., Figures 4e and 4f). For example, the coherent nearshore eddy feature in Figures 4e and 4f (at $y \approx 1250$ m and 1500 m, respectively) has an alongshore

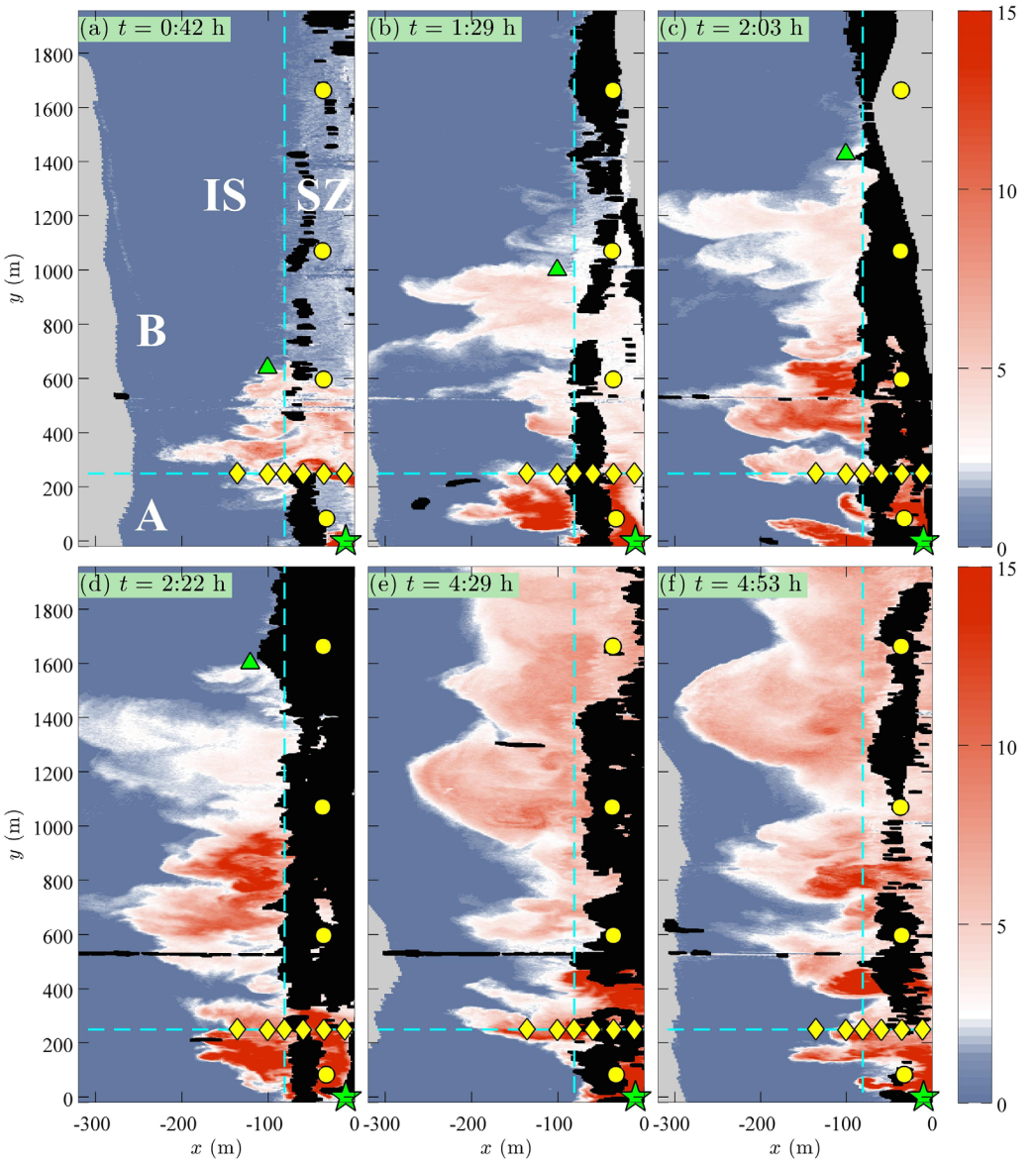

Figure 4. Aerial multispectral images of observed dye concentration D_o (ppb, see colorbar) versus cross-shore coordinate x and alongshore coordinate y for six times (indicated in each plot). The mean shoreline is at $x = 0$ m. Green star indicates location of continuous dye release (starting at $t =$ 00:00 h). Yellow diamonds indicate cross-shore array f1-f6 locations, and yellow circles indicate SA1–SA5 locations. Gray indicates regions outside the imaged area, and black indicates unresolved regions due to foam from wave breaking. Vertical cyan line at x_b divides the surfzone (SZ) and inner-shelf (IS), and horizontal cyan line at y_f divides the near and far-field regions A and B (see Figure 4a).

length scale $\approx$ 300 m, roughly six times larger than the alongshore length scales of inner-shelf dye that has been recently ejected from the surfzone (e.g., Figures 4c and 4f, ejection features at $y \leq 250$ m).

The model D_m field has similar concentrations and evolves similarly to the observed D_o field during the $\approx$ 5 h observation period (Figure 5). The D_m surfzone front propagates northward while ejecting narrow bands of dye offshore to the inner-shelf, consistent with the observations. The modeled inner-shelf dye cross-shore extent and alongshore advection rate are both similar to the observed dye. The inner-shelf D_m length scales increase with downstream distance (e.g., Figure 5f), consistent with the observed trend (e.g., Figure 4f). However, inner-shelf modeled D_m is patchier than observed D_o, with smaller alongshore length scales. While the observed dye was vertically uniform within the surfzone, observed inner-shelf dye was somewhat surface-intensified (roughly twice as strong at $z = -1$ m as at $z = -3$ m), consistent with inner-shelf thermal stratification [HR15]. When seaward rip current driven dye ejections are confined to a stratified

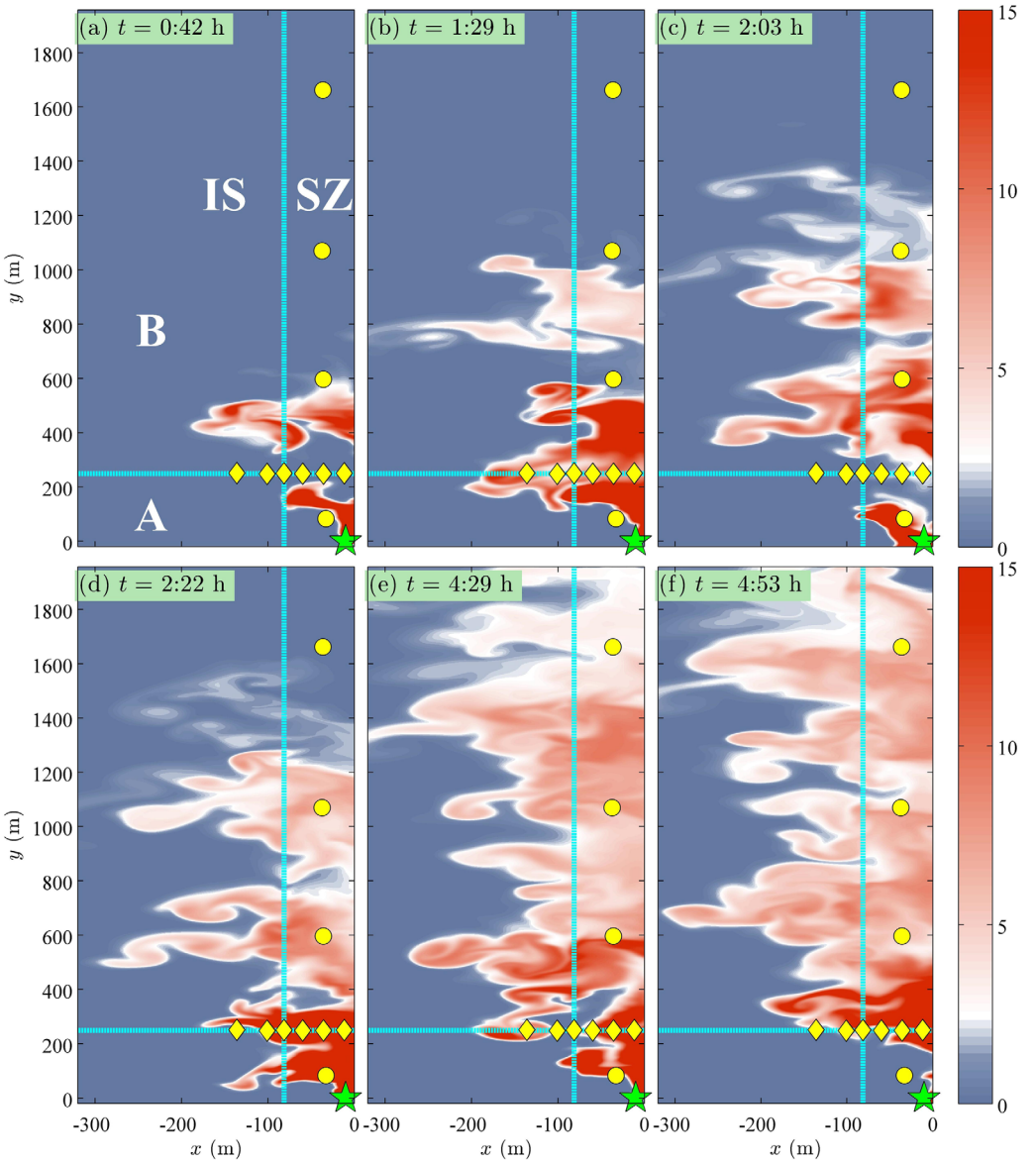

Figure 5. Planview of modeled dye concentration D_m (ppb, see colorbar) versus cross-shore coordinate x and alongshore coordinate y for six times (indicated in each plot). The mean shoreline is at $x = 0$ m. Green star indicates location of continuous dye release (starting at $t =$ 00:00 h). Yellow diamonds indicate cross-shore array f1-f6 locations, and yellow circles indicate SA1–SA5 locations. Vertical cyan line at x_b divides the surfzone (SZ) and inner-shelf (IS), and horizontal cyan line at y_f divides the near- and far-field regions A and B (see Figure 5a).

inner-shelf upper layer, dye undergoes increased lateral spreading relative to a vertically uniform tracer (e.g., funwaveC modeled dye) entering unstratified inner-shelf water [e.g., *Spydell et al.*, 2015].

3.3. Alongshore Dye Propagation

Here, the alongshore dye propagation rate is compared between the observations and model. The northward advecting dye plume leading edge is expected to be within the surfzone, where the observed and modeled mean alongshore current V is strongest (Figure 3b). However, the poor surfzone resolution of the aerial images precludes surfzone dye tracking for the observations. Instead [see HR15], the leading alongshore edge of the observed dye plume $y_{p_o}(t)$ is defined as the northernmost location where aerial-imaged inner-shelf D_o exceeds 3 ppb within 40 m of x_b, where inner-shelf dye has been recently ejected from the surfzone (e.g., Figure 4). Model $y_{p_m}(t)$ is defined analogously with D_m (e.g., Figure 5).

The observed plume leading edge $y_{p_o}(t)$ increases roughly piecewise linearly over the observation period (Figure 6, symbols) at an average rate of 0.17 m s^{-1}, consistent with in situ V_o (Figure 3b). When the dye leading edge is within the model alongshore domain ($t < 1.2\times10^4$ s), modeled $y_{p_m}(t)$ is very similar to the observed $y_{p_o}(t)$ (Figure 6, compare curve and symbols), consistent with the good agreement between observed and modeled $V(x)$. For $t > 1.2\times10^4$ s, when the model dye plume leading edge has advected beyond the northern boundary (y_{max}=1957.5 m, dashed line in Figure 6), observed $y_{p_o}(t)$ and modeled $y_{p_m}(t)$ can no longer be compared. Note the faster propagation of observed $y_{p_o}(t)$ during $t > 1.2\times10^4$ s; this is discussed in section 5.3.

3.4. Near-Shoreline Dye

Near-shoreline array (SA1–SA5) dye observations are discussed in HR15. Here, SA1–SA5 model-data time series are first compared qualitatively, followed by comparison of statistics quantifying downstream dye dilution and dye time scales.

3.4.1. Near-Shoreline Dye Time Series

Observed SA1–SA5 data begin at instrument deployment times (after the dye plume has arrived at their respective locations) and end shortly after the dye release stops (Figure 7, left column). Model SA1–SA5 results are available for all times (Figure 7, right column), and the model dye release spanned the simulation (Figure 7, magenta bars). Observed and modeled dye time series are qualitatively similar across SA1–SA5. For example, near the release at $y = 82$ m, observed D_o varies between 0 and 200 ppb with many intermittent spikes (Figure 7ao). At $y = 82$ m, the modeled D_m varies over a similar range and is also highly intermittent (Figure 7am), more so than observed. At farther downstream locations, the observed and modeled D range decreases, and the time series are less intermittent and spiked, becoming more smooth. For example, at $y = 1662$ m, observed D_o varies between 4 and 12 ppb (Figure 7eo) less rapidly that at $y = 82$ m. Similarly, modeled D_m at $y = 1662$ m varies over a comparable range (Figure 7em) and less rapidly than at smaller y.

This similarity between observed and modeled dye (Figure 7) motivates further quantitative comparison. Note, in the model D_m at $y = 1662$ m (Figure 7em), there is a clear dye ramp up period around $t=10^4$ s. In addition, the model dye release was not turned off, and there is an indication at $y = 1069$ m and $y = 1662$ m of continued increasing D_m trends at $t > 2.5\times10^4$ s (Figures 7dm and 7em). Given the good $V(x)$ (Figure 3b) and $y_p(t)$ (Figure 6) model-data agreement, near-shoreline dye tracer statistics are calculated using the same time periods for the model and the observations. Thus, quantitative model-data comparison is performed only over the observed time range at each of the SA1–SA5 (Figure 7, shaded regions).

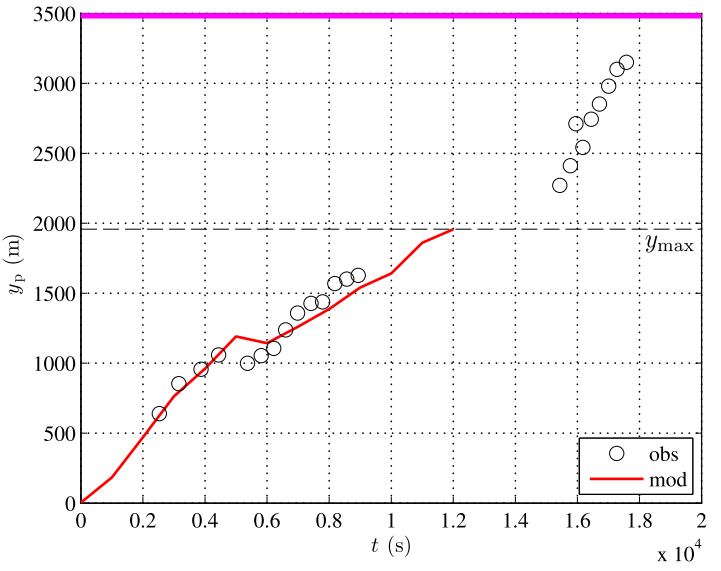

Figure 6. Observed (symbols) and modeled (curve) dye plume leading alongshore edge y_p (defined in section 3.4.2) versus time. Magenta bar indicates duration of near-shoreline, continuous dye release at $y = 0$ m (star in Figures 1 and 2). Horizontal-dashed line denotes the model domain northern boundary y_{max}.

3.4.2. Near-Shoreline Dye Alongshore Dilution

Here, the observed and modeled alongshore decay rates of near-shoreline mean dye concentration $\bar{D}$ are compared. HR15 found that the observed near-shoreline mean dye diluted downstream following a power law relationship,

$$\bar{D}=\bar{D}_0(y/y_0)^{\alpha}, \qquad (5)$$

where y_0=1 m. The least squares power law fit to the observed $\bar{D}_o$ (black-dashed line and symbols, respectively, Figure 8a) has high skill (r_o^2=0.98) with best fit constants $\bar{D}_{0_o}$=98($\pm$13) ppb and α_o= $-$0.33($\pm$0.02). The modeled near-shoreline mean $\bar{D}_m$ dilutes downstream with y in a manner very similar to the observations.

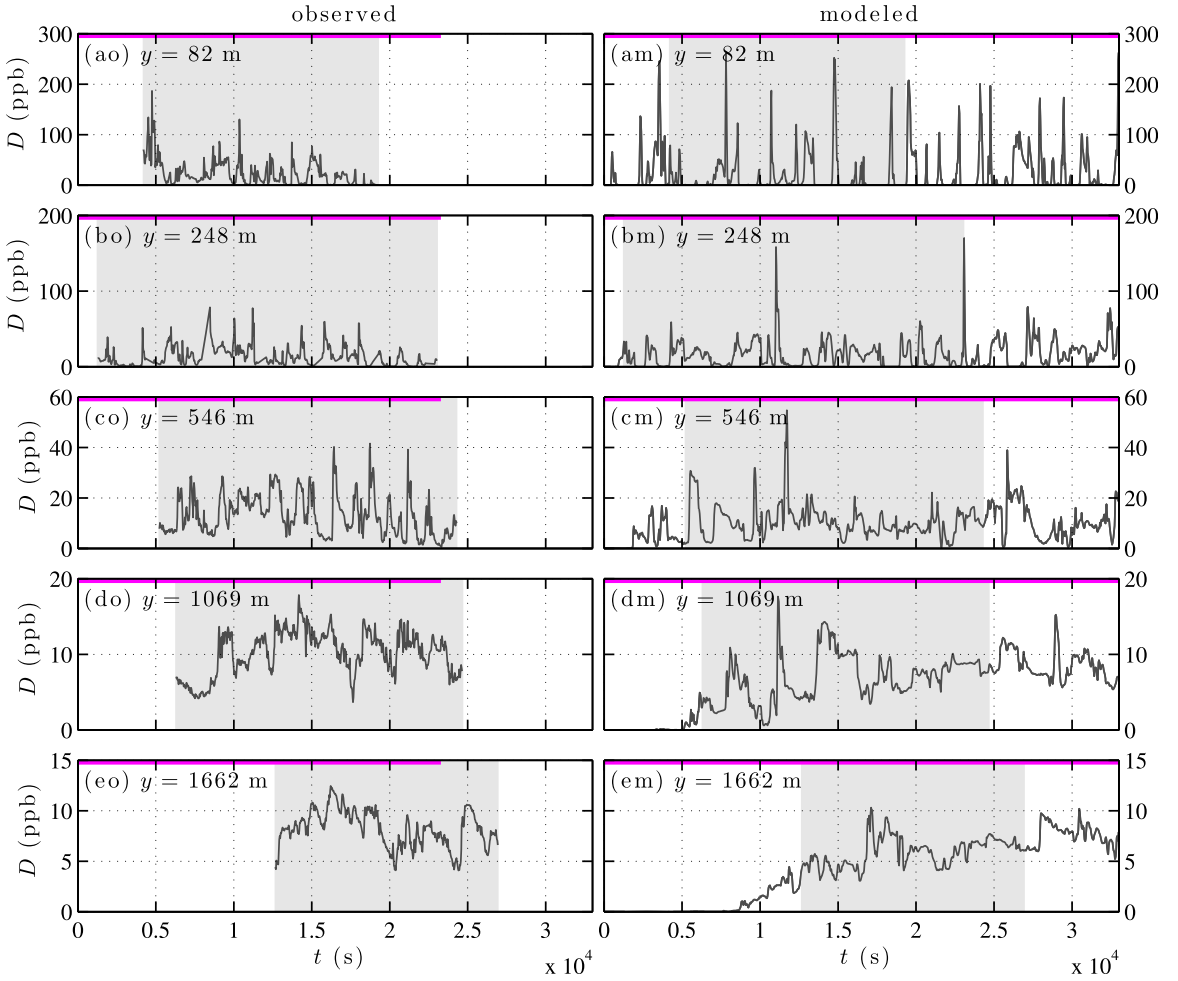

Figure 7. Observed (left) and modeled (right) dye concentration D versus time at SA1–SA5 (circles and diamond, Figures 1 and 2). Alongshore location is indicated in each plot. Magenta bars indicate duration of near-shoreline, continuous dye release at $y = 0$ m (star in Figures 1 and 2).

The least squares power-law fit to modeled $\bar{D}_m$ (red-dashed line and symbols, respectively, Figure 8a) also has high skill ($r^2_m = 0.95$), with best fit constants $\bar{D}_{0_m} = 104(\pm 30)$ ppb and $\alpha_m = -0.38(\pm 0.05)$. The observed ($\alpha_o = -0.33$) and modeled ($\alpha_m = -0.38$) power-law exponents are similar (within a standard error of each other), although the model dye dilutes slightly more rapidly. At the farthest downstream location $y_{SA5} = 1662$ m, this results in observed $\bar{D}_o = 8.2$ ppb whereas modeled $\bar{D}_m = 6.4$ ppb (Figure 8a).

Both the observed and modeled dye variability at SA1–SA5 also decrease downstream (Figure 7). The least squares power-law fit to the observed standard deviation σ_{D_o} (black-dashed line and symbols, respectively, Figure 8b) has slope -0.88. Similarly, the least squares power-law fit to the modeled standard deviation σ_{D_m} (red-dashed line and symbols, respectively, Figure 8b) has slope -1.06. The observed and modeled near-shoreline dye standard deviations are similar across SA1–SA5, although modeled σ_{D_m} is larger than the observed σ_{D_o} at the nearest location SA1 and slightly smaller than the observed σ_{D_o} at the farthest downstream location SA5 (Figure 8b).

3.4.3. Near-Shoreline Dye Time Scales

A near-shoreline dye time scale $\tilde{t}_D$ is defined as

$$\tilde{t}_D = \left[\frac{\overline{(dD'/dt)^2}}{\overline{D'^2}} \right]^{-1/2}, \tag{6}$$

where $D' = D - \bar{D}$. For observations, the $\tilde{t}_{D_o}$ are calculated using the full available time series, which span time periods when dye has equilibrated at each of the SA1–SA5 locations (Figure 7, left column). Model dye

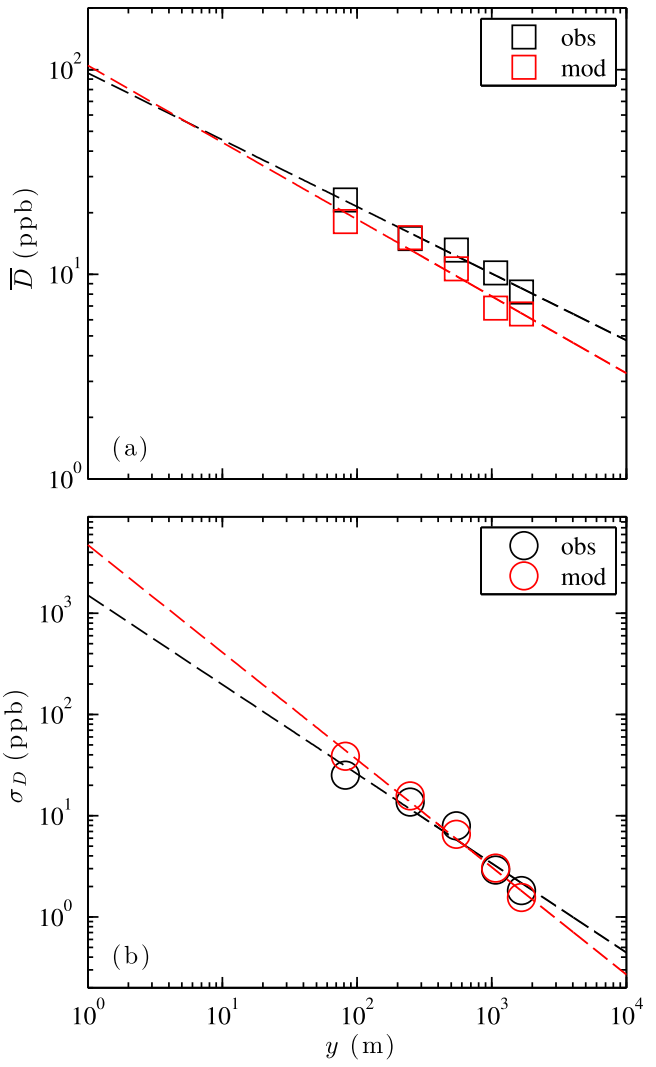

Figure 8. (a) Observed (black) and modeled (color) mean (time-averaged) dye concentration $\bar{D}$ (squares) versus alongshore coordinate y at the near-shoreline SA1–SA5 (Figures 1 and 2). Best fit lines (dashed) are $\bar{D}_o = \bar{D}_{0_o}(y/y_0)^{\alpha_o}$ and $\bar{D}_m = \bar{D}_{0_m}(y/y_0)^{\alpha_m}$ for the observations and model, respectively, with $y_0 = 1$ m. The best fit observed $\alpha_o = -0.33$ and modeled $\alpha_m = -0.38$. (b) Observed (black) and modeled (color) dye concentration standard deviation σ_D (circles) versus alongshore coordinate y at the near-shoreline SA1–SA5. Best fit σ_D power law exponents are -0.88 and -1.06 for the observations and model, respectively.

concentration time scales $\tilde{t}_{D_m}$ are calculated over the same times as the observations (Figure 7, shaded regions).

The observed $\tilde{t}_{D_o}$ increase from 53 s at SA1 to 127 s at SA5 (Figure 9, black symbols). Similarly, the modeled $\tilde{t}_{D_m}$ increase from 62 s at SA1 to 150 s at SA5 (Figure 9, red symbols). The ratio of modeled to observed $\tilde{t}_D$ is about 1.2 across all locations. This downstream increase in both $\tilde{t}_{D_o}$ and $\tilde{t}_{D_m}$ indicates a transition to larger surfzone alongshore length scales as dye concentration alongshore gradients, initially strong near the release, are reduced downstream (e.g., Figures 4 and 5) as dye is stirred and mixed by both individual bores [e.g., *Feddersen*, 2007] and surfzone eddies [e.g., *Peregrine*, 1998; *Clark et al.*, 2012; *Suanda and Feddersen*, 2015]. The downstream increase in surfzone length scales is also consistent with the downstream increase in inner-shelf length scales seen in the observed and modeled planview images (Figures 4 and 5). Such transition to longer length scales is common in a variety of turbulent environments such as flow behind a cylinder [e.g., *Tennekes and Lumley*, 1972].

3.4.4. Near-Shoreline Dye Discussion

These similarities between observed and modeled near-shoreline qualitative dye time series and quantitative dye statistics (Figures 7, 8 and 9) suggest that the model is simulating reasonably well the observed near-shoreline dye evolution, although the modeled mean $\bar{D}_m$ is slightly too small and the modeled D_m variability is somewhat too strong relative to the observations. The good model-data comparison of alongshore currents $V(x)$ (Figure 3b) and the dye plume front $y_p(t)$ (Figure 6) indicate that the alongshore dye advection is well simulated. Together, this suggests that the model is ejecting dye from the surfzone to the inner-shelf realistically as well, consistent with the similarities of the observed and modeled planview dye maps (Figures 4 and 5).

3.5. Cross-Shore Dye Profiles

From Huntington Beach 2007 releases, *Clark et al.* [2011] showed reasonable agreement between observed and funwaveC-modeled cross-shore dye profiles within the surfzone, but no farther than 160 m offshore and no farther than 225 m downstream of the dye source. Here, jetski-observed (surface) and modeled (depth-averaged) mean dye cross-shore profiles are compared up to 350 m offshore and roughly 1700 m downstream. For this comparison, the jetski-observed surface dye $D_o^s(x)$ must be normalized to a depth-average. The observed dye was vertically well mixed in the surfzone [HR15], while inner-shelf dye was surface-intensified with a vertical scale such that the observed depth-normalized dye

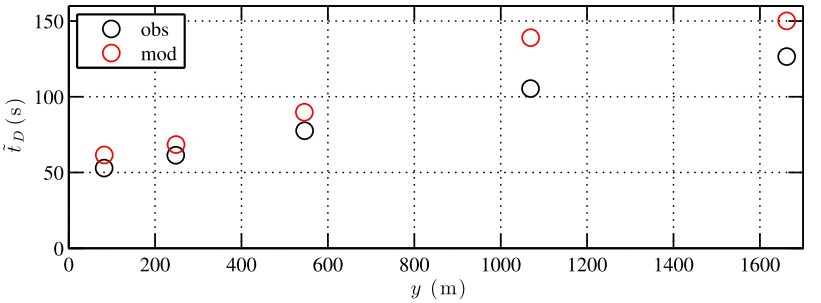

Figure 9. Observed (black) and modeled (color) dye time scale $\bar{t}_D$ (6) versus alongshore coordinate y.

$$D_o(x) = \left(\frac{h_{dye}}{h}\right) D_o^s(x), \tag{7}$$

where $h_{dye}(x) = \min(h(x), 2.7\,\mathrm{m})$ [HR15].

Mean observed cross-shore dye profiles $\langle D_o(x)\rangle$ are calculated by averaging the repeated jetski cross-shore transects at alongshore locations y_j closest to the SA locations, with transects subsampled for times during the SA observation periods (Figure 7, left column). The jetskis were driven as far onshore as possible but were unable to sample all the way to the mean shoreline. Mean modeled cross-shore dye profiles $\langle D_m(x)\rangle$ at the SA1–SA5 alongshore locations are averaged during the observed time periods (Figure 7, shaded), when model dye had equilibrated at each SA location. The Δy between jetski transects and SA locations was typically $<2\%$ of the downstream distance y, except at SA2 where $\Delta y = 40$ m. No model-data comparison is made for SA3 (just north of the Imperial Beach pier), as the jetskis could not operate safely near this location.

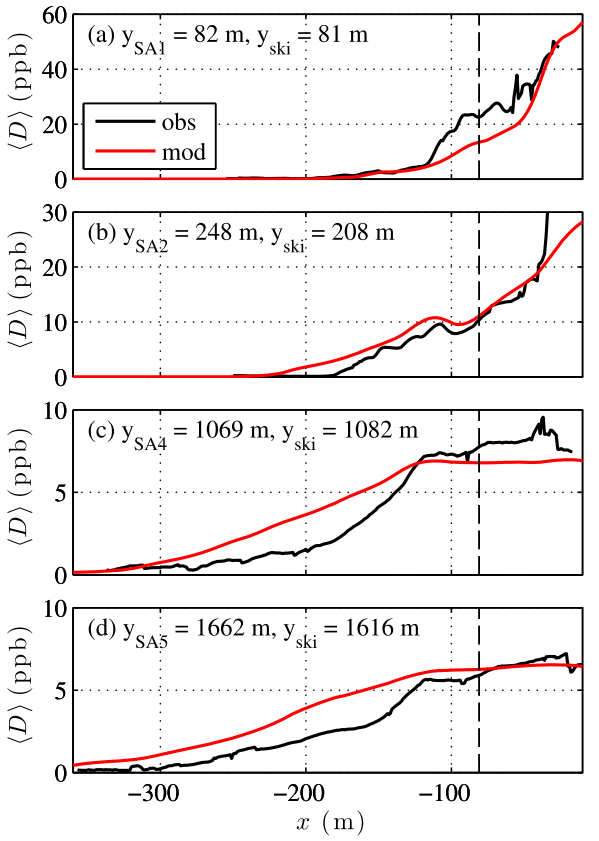

Figure 10. Observed (black) and modeled (color) mean dye concentration $\langle D\rangle$ versus cross-shore coordinate x at select alongshore locations y (for the model, the SA1–SA5 y locations; for the observations, the jetski transect locations y_j nearest SA1–SA5). Vertical-dashed line denotes the surfzone/inner-shelf boundary x_b.

At SA1 ($y = 82$ m), observed $\langle D_o(x)\rangle$ has a near-shoreline maximum of 50 ppb and decays across the surfzone (Figure 10a, black). At the surfzone/inner-shelf boundary x_b (Figure 10a, dashed vertical line), $\langle D_o\rangle \approx 25$ ppb. Roughly 30 m offshore on the inner-shelf, observed dye decays to $\langle D_o\rangle < 5$ ppb. The modeled $\langle D_m(x)\rangle$ has a similar near-shoreline maximum and decays rapidly offshore (Figure 10a, red). Near x_b, the modeled $\langle D_m\rangle$ is weaker than observed. However, offshore of $x \approx -120$ m, the modeled $\langle D_m\rangle$ and observed $\langle D_o\rangle$ are again similar, as near the shoreline. At SA2 ($y = 248$ m), observed $\langle D_o(x)\rangle$ has diluted near the shoreline (with a maximum of 30 ppb), and has spread farther offshore onto the inner-shelf (Figure 10b, black). The SA2 modeled $\langle D_m(x)\rangle$ is similar to the observed, both in the surfzone and inner-shelf regions (Figure 10b, red). Farther downstream at SA4 ($y = 1069$ m), the observed $\langle D_o(x)\rangle$ is roughly uniform

across the surfzone [as in HR15] and out to $x \approx -120$ m (about $1.5x_b$, Figure 10c, black). Offshore of $x \approx -120$ m, observed $\langle D_o(x) \rangle$ decreases to $\langle D_o \rangle < 1$ ppb at $x < -300$ m, consistent with the planview aerial images (Figure 4). Similarly, SA4 modeled $\langle D_m(x) \rangle$ is also cross-shore uniform from the shoreline to roughly $1.5x_b$ (Figure 10c, red), with magnitude slightly less than observed. Offshore, modeled dye decays to $\langle D_m \rangle < 1$ ppb at $x < -300$ m as in the observations, but the inner-shelf modeled dye decays less rapidly than observed. At the farthest downstream location SA5 ($y = 1662$ m), observed $\langle D_o(x) \rangle$ has further slowly diluted at the shoreline, is again cross-shore uniform out to roughly $1.5x_b$ (Figure 10d, black), and decays offshore in a manner similar to the SA4 observed cross-shore decay. The SA5 modeled $\langle D_m(x) \rangle$ is also well mixed out to $x \approx -120$ m (Figure 10d, red), but as at SA4, the SA5 modeled $\langle D_m(x) \rangle$ decays less quickly than observed.

The $\langle D(x) \rangle$ model-data agreement close to the release ($y < 250$ m), where dye is largely surfzone-contained (Figures 10a and 10b), shows that the model accurately reproduces surfzone cross-shore tracer dispersion. Farther downstream ($y > 1000$ m), where dye is spread cross-shore well beyond the surfzone boundary, the inner-shelf has somewhat more dye in the model than in the observations (Figures 10c and 10d). Averaged over the SA locations, the inner-shelf has 26% more cross-shore integrated dye in the model than the observations, though the modeled and observed $\langle D(x) \rangle$ decay scales remain similar.

3.6. Alongshore Dye Transport

Observed and modeled cumulative alongshore dye transports are compared at the cross-shore frame array $y_f = 248$ m during the observed dye release time period. The alongshore transport $\mathcal{T}^{y_f}$ from region A to region B (see Figure 4a) is defined [HR15] for the surfzone,

$$\mathcal{T}^{y_f}_{SZ}(t) = \int_{x_b}^{0} d(x,t)V(x,t)D(x,t)\,dx, \tag{8}$$

and the inner-shelf,

$$\mathcal{T}^{y_f}_{IS}(t) = \int_{x_{f6}}^{x_b} d(x,t)V(x,t)D(x,t)\,dx. \tag{9}$$

The surfzone and inner-shelf alongshore transports are estimated using 30 s averaged total water depth $d = h + \eta$, alongshore current V, and dye concentration D. For the observations, (8) and (9) are estimated with measurements from the near-bottom frames f1-f6 (Figure 3c), where $V_o(x,t)$ and $D_o(x,t)$ are assumed vertically uniform, and cross-shore integration is performed with the trapezoid rule. Model V_m and D_m are available at all x and are vertically uniform throughout the domain.

The observed and modeled alongshore dye transports (8) and (9) fluctuate significantly (not shown here; see HR15 for observed), consistent with the observed and modeled $D(t)$ fluctuations (e.g., at f2/SA2; Figures 7bo and 7bm). Here, the cumulative (time-integrated) alongshore transports $\int_0^t \mathcal{T}^{y_f}(\tau)\,d\tau$ are compared between the observations and model for the surfzone and inner-shelf regions separately and together. The observed cumulative surfzone alongshore transport $\int_0^t \mathcal{T}^{y_f}_{SZ_o}\,d\tau$ increases approximately linearly (Figure 11, gray dashed) and at the end of the observed dye release ($t = 2.3\times10^4$ s) totals 62% of the released dye. The corresponding release-averaged $\overline{\mathcal{T}}^{y_f}_{SZ_o} = 320$ ppb m^3 s^{-1}. The modeled cumulative surfzone alongshore transport $\int_0^t \mathcal{T}^{y_f}_{SZ_m}\,d\tau$ is similar to the observed for $t < 1.2\times10^4$ s, and becomes less than the observed for $t > 1.2\times10^4$ s (Figure 11, compare gray solid and dashed). At the end of the observed release, the modeled surfzone $\int_0^t \mathcal{T}^{y_f}_{SZ_m}\,d\tau$ is roughly three quarters of the observed surfzone $\int_0^t \mathcal{T}^{y_f}_{SZ_o}\,d\tau$. For the inner-shelf, the observed $\int_0^t \mathcal{T}^{y_f}_{IS_o}\,d\tau$ is also approximately linear (Figure 11, blue dashed) and at the end of the release reaches 15% of the total released dye. The corresponding release-averaged inner-shelf $\overline{\mathcal{T}}^{y_f}_{IS_o} = 76$ ppb m^3 s^{-1}, roughly one quarter of the mean observed surfzone $\overline{\mathcal{T}}^{y_f}_{SZ_o}$. The modeled cumulative inner-shelf alongshore transport $\int_0^t \mathcal{T}^{y_f}_{IS_m}\,d\tau$ is similar to the observed for $t < 1.2\times10^4$ s and becomes greater than observed thereafter (Figure 11, compare blue solid and dashed). At the end of the observed dye release, the modeled inner-shelf $\int_0^t \mathcal{T}^{y_f}_{IS_m}\,d\tau$ is approximately twice the observed inner-shelf $\int_0^t \mathcal{T}^{y_f}_{IS_o}\,d\tau$.

Overall, the total (surfzone + inner-shelf) cumulative alongshore transports ($\int_0^t \left(\mathcal{T}^{y_f}_{SZ} + \mathcal{T}^{y_f}_{IS}\right) d\tau$) are very similar for the observations and the model (Figure 11, compare black-dashed and solid curves). The smaller modeled surfzone alongshore transport is compensated by a larger modeled inner-shelf alongshore transport. The model-data surfzone alongshore transport difference is consistent with weaker mean surfzone

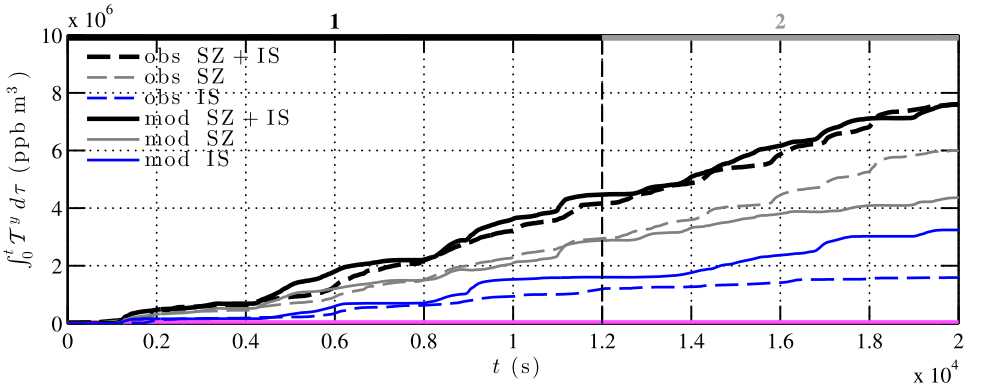

Figure 11. Observed (dashed) and modeled (solid) cumulative (time-integrated) alongshore dye transports at $y_f = 248$ m versus time. Observed and modeled dye was released near the shoreline at $y = 0$ m (Figures 1 and 2) throughout this time period (magenta bar). Vertical-dashed line separates periods 1 and 2.

dye concentrations in the model than in the observations (e.g., Figures 8 and 10). For the inner-shelf, the model-data alongshore transport difference could be due to model-data differences in region A surfzone to inner-shelf ejection rates or to a low-biased estimation of (9) for the observations. These differences are further discussed in sections 5.2 and 5.3.

4. Dye Mass Balances and Surfzone/Inner-Shelf Exchange

In section 3, both qualitative and quantitative model-data dye comparisons are good, motivating examination of dye mass budgets and surfzone/inner-shelf exchange. HR15 closed the first coupled surfzone and inner-shelf dye budget. Over roughly 5 h and 3.2 km downstream, approximately 1/2 of the shoreline-released dye was observed to be transported offshore from the surfzone to the inner-shelf [HR15]. This transport was parameterized well using a bulk exchange velocity and mean surfzone to inner-shelf dye concentration difference [HR15]. Here, a model dye mass budget is examined and compared to the observations.

Surfzone and inner-shelf dye masses over the alongshore model domain are defined for both the observations and the model as

$$M_{SZ}(t) = \int_{y_{\min}}^{y_{\max}} \int_{x_b}^{0} \int_{-h}^{\eta} D(x,y,z,t)\, dz\, dx\, dy, \tag{10}$$

and

$$M_{IS}(t) = \int_{y_{\min}}^{y_{\max}} \int_{x_{\text{off}}}^{x_b} \int_{-h}^{\eta} D(x,y,z,t)\, dz\, dx\, dy, \tag{11}$$

where x_{off} is the offshore boundary of the aerial observations (e.g., Figure 4) or the offshore model tracer domain boundary (Figure 2, heavy-dashed line), and the alongshore integration limits $y_{\min} = -67.5$ m and $y_{\max} = 1957.5$ m correspond to the model domain. HR15 developed a methodology for estimating observed M_{SZ_o} and M_{IS_o}, calculated over the full observed alongshore extent of the dye plume, up to 3.2 km downstream (e.g., Figure 6). Here, the observed surfzone M_{SZ_o} and inner-shelf M_{IS_o} are recalculated using the HR15 methodology, but with alongshore integration limits restricted to the model domain $(y_{\min}, y_{\max})$. The observed dye mass estimates are available only at the times of the aerial images (e.g., Figure 4) spanning roughly $t = (0.2-1.8)\times10^4$ s (e.g., Figure 6, symbols). Modeled dye masses are directly calculated from the vertically averaged, highly resolved (x, y, t) model output (section 2.2.1).

For the purposes of observed and modeled dye mass balance analysis, the time period $t = 0-2\times10^4$ s is separated into two. Period 1 ($t < 1.2\times10^4$ s) is the time prior to the observed and modeled dye plumes reaching the alongshore extent of the model domain (Figure 6), and period 2 ($t > 1.2\times10^4$ s) is the time after observed and modeled dye begins advecting beyond this region.

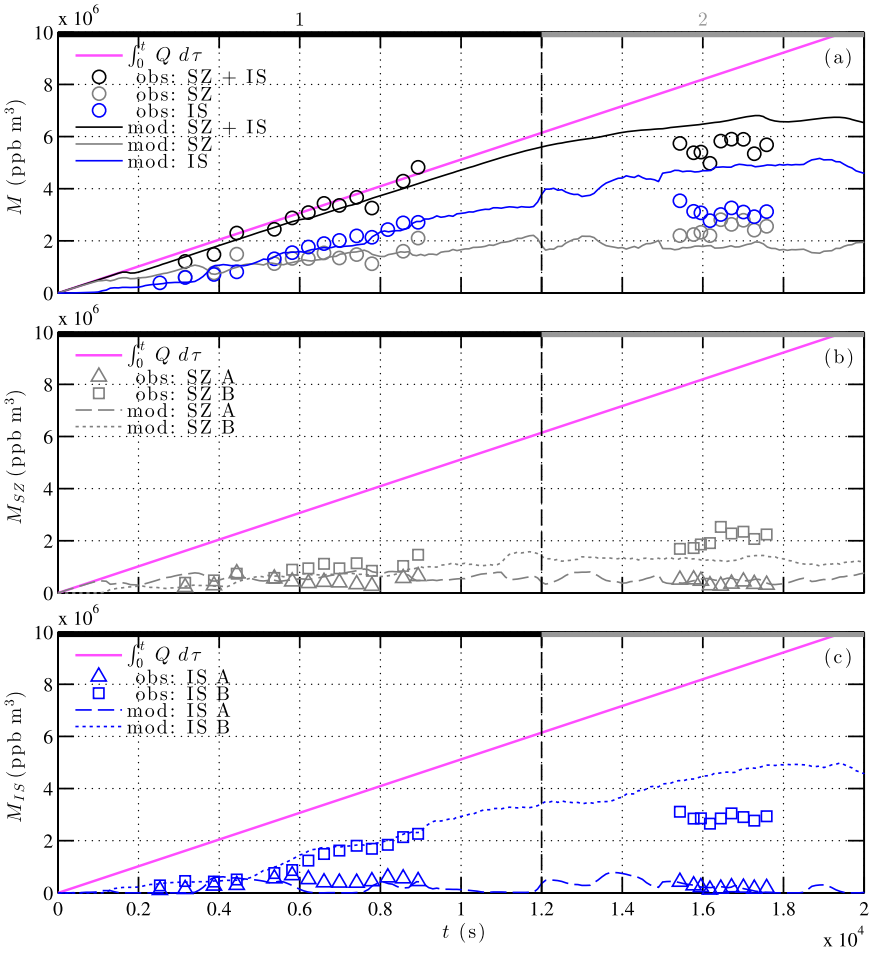

Figure 12. Observed (symbols) and modeled (curves) surfzone and inner-shelf dye masses for regions A and B versus time. Magenta line shows the cumulative dye mass released near the shoreline. Vertical-dashed line denotes the time when the observed and modeled dye plumes advect beyond the model domain (Figure 6), defining periods 1 and 2, noted above Figure 12a.

4.1. Dye Mass Balance: Total, Surfzone, and Inner-Shelf

The total dye mass balance for the surfzone and inner-shelf is

$$M_{SZ}(t)+M_{IS}(t)=\int_0^t Q\,d\tau, \tag{12}$$

where Q=512 ppb m^3 s^{-1} is the steady dye release rate starting at $t=0$ s, and $M_{SZ}=M_{IS}=0$ ppb m^3 at $t=0$ s. The observed total dye mass balance (12) closes within 10% during period 1 (Figure 12a, compare black symbols and magenta line). During period 2 when the dye plume extends beyond $y_{max,}$ the total observed dye mass within $y_{min} \le y \le y_{max}$ levels off at ≈ 70% of the cumulative released dye mass (Figure 12a). The modeled total dye mass balance also closes well during period 1 (Figure 12a, compare black curve and magenta line). A small fraction (<10%) of model total dye mass is lost at the upstream (southern) boundary y_{min} when near-release eddies recirculate dye southward. Similar to the observations, the rate of increasing modeled total dye mass slows during period 2, as dye being released into the domain is offset by dye alongshore-advecting out of the domain through y_{max}.

Early in period 1, the observed $M_{SZ_o} \approx M_{IS_o}$ (Figure 12a, gray and blue symbols). Starting later in period 1, as more dye spreads from the surfzone to the inner-shelf, the observed M_{IS_o} becomes larger than M_{SZ_o}. During period 2, both M_{SZ_o} and M_{IS_o} level off due to dye propagating beyond y_{max}, with the observed dye mass remaining larger for the inner-shelf than the surfzone (Figure 12a, gray and blue symbols). For the model, $M_{SZ_m} > M_{IS_m}$ for roughly the first hour of the release (Figure 12a, gray and blue curves, respectively), as expected with a surfzone dye source. For the remainder of period 1, modeled $M_{IS_m} > M_{SZ_m}$, with both inner-

shelf and surfzone modeled dye mass magnitudes very similar to the observations (Figure 12a, blue and gray curves and symbols during period 1). However, during period 2, the inner-shelf modeled dye mass is larger than observed ($M_{IS_m} > M_{IS_o}$, Figure 12a, blue curve and symbols, respectively), while the surfzone modeled dye mass is smaller than observed ($M_{SZ_m} < M_{SZ_o}$, Figure 12a, gray curve and symbols, respectively). Overall, the total, surfzone, and inner-shelf dye masses are very similar for the model and the observations during period 1, and less similar during period 2 (Figure 12a, compare curves with symbols). The period 2 differences are discussed in section 5.3.

4.2. Near and Far-Field Dye Masses

As in HR15, the observed and modeled domains are partitioned alongshore into the near-field region A ($y \leq y_f$) and the far-field region B ($y > y_f$), where $y_f = 248$ m. For the observed surfzone dye masses, during the early portion of period 1 when dye has not advected very far downstream (e.g., Figures 4a and 6), $M^A_{SZ_o}$ and $M^B_{SZ_o}$ are comparable (Figure 12b, symbols). As dye moves farther downstream during period 1 (e.g., Figures 4b–4d and 6), observed $M^B_{SZ_o}$ becomes larger than $M^A_{SZ_o}$. Though dye concentrations are highest near the release (region A), the observed downstream power law decay (5) is relatively weak ($\alpha_o = -0.33$), and the larger alongshore extent of the dye plume in region B than region A results in $M^B_{SZ_o} \approx 2M^A_{SZ_o}$ (Figure 12b, symbols). During period 2 when dye has advected > 2 km downstream (e.g., Figures 4e, 4f, and 6), the observed $M^B_{SZ_o} \approx 4M^A_{SZ_o}$ (Figure 12b, symbols). For the modeled surfzone dye masses early in period 1, $M^A_{SZ_m} > M^B_{SZ_m}$ (Figure 12b, curves), as dye has not yet advected far downstream (e.g., Figures 5a and 6). As dye moves farther downstream in period 1 (e.g., Figures 5b–5d and 6), modeled $M^B_{SZ_m} \approx M^A_{SZ_m}$, with $M^A_{SZ_m}$ somewhat greater than observed, and $M^B_{SZ_m}$ somewhat less than observed (Figure 12b, curves and symbols). For period 1, modeled and observed M_{SZ} are similar in both region A and region B. During period 2, modeled $M^A_{SZ_m}$ is similar to observed $M^A_{SZ_o}$ (Figure 12b, dashed curve and triangles), but $M^B_{SZ_m} < M^B_{SZ_o}$ (Figure 12b, dotted curve and squares), resulting in a period 2 modeled mean ratio $\overline{M^B_{SZ_m}/M^A_{SZ_m}}$ smaller than the corresponding observed ratio $\overline{M^B_{SZ_o}/M^A_{SZ_o}}$ (Figure 12b, compare curves and symbols).

For the inner-shelf observations (Figure 12c, symbols), period 1 and period 2 ratios $M^B_{IS_o}/M^A_{IS_o}$ both follow similar trends to, but are larger than, the observed surfzone ratios $M^B_{SZ_o}/M^A_{SZ_o}$. Early in period 1, $M^A_{IS_o} \approx M^B_{IS_o}$. Later in period 1, $M^B_{IS_o}$ increases while $M^A_{IS_o}$ remains approximately constant. During period 2, observed $M^B_{IS_o} \gg M^A_{IS_o}$ (Figure 12c, symbols). During period 1, the modeled and observed inner-shelf dye masses M_{IS} are similar in both region A and B (Figure 12c, compare symbols and curves). Early in period 1, modeled inner-shelf dye masses M_{IS_m} are similar for regions A and B, as observed. Later in period 1, modeled $M^B_{IS_m}$ increases at a rate consistent with observed $M^B_{IS_o}$ (Figure 12c, dotted curve and squares), while $M^A_{IS_m}$ remains nearly constant as in the observations (Figure 12c, dashed curve and triangles). During period 2, modeled $M^A_{IS_m}$ remains small and comparable to observed $M^A_{IS_o}$, while modeled $M^B_{IS_m}$ continues increasing, becoming larger than observed $M^B_{IS_o}$ (Figure 12c). This leads to period 2 total (A+B) modeled M_{IS_m} larger than total observed M_{IS_o} (Figure 12a, compare blue curve and symbols).

4.3. Cross-Shore Surfzone/Inner-Shelf Exchange

Because the observed and modeled dye mass budgets close during period 1 (Figure 12a and Section 4.1), the inner-shelf dye mass can be used to calculate the surfzone to inner-shelf cross-shore transport of shoreline-released dye. At any time, the total inner-shelf dye mass must equal the cumulative (time-integrated) cross-shore transport input from the surfzone and the cumulative inner-shelf alongshore transport loss through y_{max}, i.e.,

$$\int_0^t \mathcal{T}^x_{SZ/IS}(\tau)\, d\tau = M_{IS}(t) + \int_0^t \mathcal{T}^{y_{max}}_{IS}(\tau)\, d\tau. \tag{13}$$

During period 1, before $y_p(t)$ has reached y_{max} (Figure 6), the inner-shelf alongshore transport $\mathcal{T}^{y_{max}}_{IS}$ is zero. Therefore, the period 1 cross-shore transport $\mathcal{T}^x_{SZ/IS} = \frac{d}{dt}(M_{IS})$ and can be estimated via the best fit slope of inner-shelf dye mass M_{IS}. In period 1, the observed and modeled inner-shelf total dye masses agree very well (Figure 12a, compare blue symbols and blue curve). The period 1 observed and modeled cross-shore transports $\mathcal{T}^x_{SZ/IS}$ are calculated via the least squares slopes of observed and modeled M_{IS}, respectively, during times spanning the inner-shelf dye mass observations ($t = (2.5-8.9)\times 10^3$ s, Figure 12a, blue symbols and blue curve). The resulting period 1 observed and modeled cross-shore transports ($\mathcal{T}^x_{SZ/IS_o} = 382$ ppb m^3 s^{-1} and $\mathcal{T}^x_{SZ/IS_m} = 349$ ppb m^3 s^{-1}) agree within 10%. This period 1 model-data $\mathcal{T}^x_{SZ/IS}$ agreement suggests that the

transient rip currents of funwaveC realistically simulate cross-shore surfzone/inner-shelf tracer exchange for alongshore-uniform bathymetry and the observed wave conditions.

5. Discussion

5.1. Mechanisms of Surfzone/Inner-Shelf Exchange

For alongshore-uniform bathymetries, potential surfzone/inner-shelf cross-shore tracer exchange mechanisms include transient rip currents [e.g., *Hally-Rosendahl et al.*, 2014; *Suanda and Feddersen*, 2015], internal waves [e.g., *Sinnett and Feddersen*, 2014], and Stokes-drift-driven flow [e.g., *Lentz et al.*, 2008]. Based on the 13 October observed dye, dye mass budgets, and inferred exchange velocity magnitude, HR15 showed that the observed surfzone/inner-shelf dye exchange on this day with moderate waves was dominated by transient rip currents. The depth-averaged funwaveC model includes this mechanism but does not include internal waves or Stokes-drift driven exchange. The good model-data M_{IS} agreement in all regions (Figure 12) implies that the model accurately reproduces the observed cross-shore surfzone/inner-shelf exchange $\mathcal{T}^{x}_{SZ/IS_o}$, confirming that transient rip currents were the dominant exchange mechanism within 3 surfzone widths of the shoreline during the observed 5 h time period. Over longer time scales or farther offshore of the surfzone, internal waves [e.g., *Suanda et al.*, 2014; *Walter et al.*, 2014], Stokes-drift-driven flow [e.g., *Lentz et al.*, 2008], or other inner-shelf processes may become important.

5.2. Inner-Shelf Stratification and Vertical Variation

HR15 showed that the 13 October dye field was vertically uniform within the surfzone. However, inner-shelf dye was surface-intensified (see Figure 13 in HR15) with a vertical dye scale $h_{\mathrm{dye}}=2.7$ m, potentially due to inner-shelf thermal stratification. The vertically integrated Boussinesq and tracer models lack stratification and vertical dye variation. Although the overall model-data agreement is good, the model's lack of vertical variation might be important for particular inner-shelf model-data differences.

For example, modeled inner-shelf D_{m} is patchier than the observed inner-shelf D_{o} (compare Figures 4 and 5). Consider a fluid column of dye ejected by a rip current from the surfzone onto the deeper inner-shelf. If the ejection is confined to an upper layer by inner-shelf stratification [e.g., HR14; HR15], it would be expected to undergo greater lateral spreading (resembling elevated lateral mixing) relative to an ejection that is able to stretch vertically over the entire water column as it moves offshore (e.g., funwaveC modeled dye). This stratified upper layer spreading mechanism explains the difference in observed and modeled lateral spreading of drifters leaving a tidal inlet [e.g., *Spydell et al.*, 2015], and may explain the difference in patchiness between the observed and funwaveC modeled inner-shelf dye.

Vertical variation might also be important for the inner-shelf dye mass and alongshore transport $\mathcal{T}^{y_f}_{IS}$ model-data difference. Although the total (surfzone + inner-shelf) cumulative alongshore transports are similar for the observations and the model (Figure 11, compare black-dashed and solid curves), this is due in part to the opposing differences for the surfzone and the inner-shelf (Figure 11, compare dashed and solid gray and blue curves, respectively). The smaller modeled surfzone dye mass and alongshore transport are consistent with weaker near-shoreline mean dye concentrations in the model than in the observations (e.g., Figures 8 and 10). For the inner-shelf, the larger modeled dye mass and alongshore transport could imply that region A dye is ejected offshore of the surfzone more quickly in the model than in the observations. However, as the D_{o} and V_{o} used in (9) are near-bottom measurements, another possible explanation for smaller observed $\mathcal{T}^{y_f}_{IS_o}$ is the low bias due to observed vertical variation of inner-shelf D_{o} [HR15] and potential vertical variation of inner-shelf V_{o}.

5.3. Additional Considerations

Overall, the surfzone and inner-shelf dye model-data agreement is quite good. Here, specific model and analysis choices that might affect the model-data comparison are discussed. The wind and wave field are stationary in the model, while the observed wind and wave field did evolve somewhat, as did the observed alongshore current V_{o} (note the faster $y_{\mathrm{p_o}}(t)$ propagation for $t > 1.2\times10^4$ s, Figure 6). This might contribute to the larger observed than modeled surfzone alongshore transport during period 2 (Figure 11, compare gray-dashed and solid curves). However, the general model-data agreement indicates that the stationary wave and wind field in the model is a reasonable approximation, particularly for $t < 1.2\times10^4$ s.

In addition, the model bathymetry is perfectly alongshore-uniform, while the observed bathymetry had some weak alongshore nonuniformities. Nevertheless, the model-data dye agreement suggests that use of an alongshore-uniform model bathymetry is reasonable. Future modeling studies will examine the relative importance of bathymetrically controlled rip currents [e.g., *Castelle and Coco*, 2013; *Castelle et al*., 2014] versus transient rip currents in driving surfzone to inner-shelf exchange.

Next, the model has no tidal variation. The observed low tide occurred at $t=6.8\times10^3$ s (roughly midway through period 1) and rose by $\approx$ 0.7 m by the end of period 2. While the surfzone/inner-shelf boundary x_b is fixed and identical in both the model and observations, the true observed surfzone/inner-shelf boundary may have shifted onshore by $\approx$ 20 m, potentially biasing the observed period 2 surfzone and inner-shelf dye masses high and low, respectively. This could also explain in part the differences between observed and modeled alongshore dye transports (Figure 11). If the model had a rising tide with a fixed x_b, this could result in larger modeled surfzone transport and smaller modeled inner-shelf transport, more closely matching the period 2 observations.

The model background diffusivity $\kappa_0=0.075\,\mathrm{m^2\,s^{-1}}$ is small relative to the surfzone breaking-wave and eddy-induced diffusivity. Although some inner-shelf background diffusivity is expected, a priori κ_0 may not be insignificant relative to the inner-shelf diffusivity induced by wave and eddy processes. However, over the $\approx 1.2\times10^4$ s duration that a tracer parcel is within the model domain (Figure 6), κ_0 disperses an initial delta function to $\approx$ 40 m length scales, small relative to the observed and modeled $\approx$ 200 m inner-shelf cross-shore scales near the end of the domain (Figures 4 and 5). Furthermore, background diffusivity does not generate the inner-shelf alongshore-patchy dye structure (Figures 4 and 5). Thus, the background diffusivity is not expected to have a significant impact on inner-shelf tracer dispersion.

Last, for idealized normally incident waves and planar bathymetries, funwaveC transient rip current driven exchange velocities depend strongly on wave height and directional spread [*Suanda and Feddersen*, 2015]. In these idealized simulations, the exchange velocity maxima increased with wave directional spread, suggesting that the observed and modeled dye releases examined here may each have had different surfzone to inner-shelf exchange rates if the directional spread were much larger or smaller. Future studies will examine how modeled cross-shore tracer exchange depends on incident wave conditions for realistic bathymetries and wave fields.

6. Summary

A near-shoreline, continuous 6.5 h dye release on 13 October 2009 at the approximately alongshore-uniform Imperial Beach, CA (IB09 experiment) [see HR15] is simulated with the wave-resolving Boussinesq model funwaveC. The model generates surfzone vorticity and transient rip currents driven by finite crest length wave breaking. However, the depth-averaged model does not resolve stratification or vertical dye variation, which are potentially important on the inner-shelf. Here we compare the observed and modeled surfzone and inner-shelf dye dispersion and cross-shore exchange.

The funwaveC model is initialized with the alongshore-averaged Imperial Beach bathymetry and the 13 October observed wave spectrum and mean wind. The model reproduces the observed inner-shelf and surfzone significant wave height and alongshore current. Both qualitative and quantitative model-data agreement for dye is good. Observed and modeled surfzone dye advects alongshore at similar rates while being intermittently ejected offshore onto the inner-shelf. The narrow inner-shelf dye features evolve to larger length scales as they advect downstream, with modeled dye somewhat patchier than observed. Over 1700 m alongshore, near-shoreline mean dye concentration decays downstream following a power law relationship with similar observed (-0.33) and modeled (-0.38) exponents. Observed and modeled near-shoreline dye time scales increase similarly with downstream distance, consistent with the inner-shelf downstream evolution to larger dye length scales. Mean cross-shore dye profiles are similar for the observations and the model, with near-release dye strongest at the shoreline and decaying rapidly offshore. Farther downstream ($>$1000 m), observed and modeled profiles widen, with dye cross-shore well mixed out to 1.5 surfzone widths from the shoreline. On the inner-shelf, the depth-normalized observed cross-shore dye profiles decay more quickly than the modeled profiles, but the observed and modeled cross-shore decay scales are similar. Surfzone and inner-shelf alongshore dye transports are each well modeled early in the release,

while they are under and overpredicted, respectively, later in the release. The total alongshore dye transport is well modeled at all times.

Modeled and observed dye mass budgets over the model domain ($\approx$ 2 km alongshore) are very similar to each other for times $<$ 3.5 h, before observed and modeled dye begin advecting out of the domain. During this time, the observed and modeled dye budgets each close to within 10% and have very similar distributions of surfzone and inner-shelf dye mass. Cross-shore dye transports for the observations and the model agree within 10%. Later in the release, after dye begins advecting beyond the model domain, total observed, and modeled dye masses still agree fairly well, although modeled dye mass is underpredicted in the surfzone and overpredicted on the inner-shelf. Model-data differences may be due to the model's lack of inner-shelf stratification and vertical dye variation or the model's lack of tide, biasing the location of the surfzone/inner-shelf boundary.

Overall, the good model-data agreement indicates that the wave-resolving, depth-averaged Boussinesq model funwaveC accurately reproduces nearshore tracer transport and dispersion over 5 h and 2000 m for approximately alongshore-uniform bathymetry during moderate wave conditions. This confirms that transient rip currents are the dominant mechanism of the observed surfzone/inner-shelf cross-shore tracer exchange, and suggests that funwaveC realistically reproduces the intensity, frequency, and scales of the observed transient rip currents.

Acknowledgments

IB09 field work and analysis was funded by ONR Littoral Geosciences and Optics, NSF, and California Sea Grant. K. Hally-Rosendahl was supported by the National Science Foundation Graduate Research Fellowship under grant DGE1144086 and California Sea Grant under Project No. R/CONT-207TR. Staff and students from the Integrative Oceanography Division (B. Woodward, B. Boyd, K. Smith, D. Darnell, R. Grenzeback, A. Gale, R. T. Guza, D. Clark, M. Spydell, M. Omand, M. Yates, M. Rippy, A. Doria), L. Lenain, and D. Castel were instrumental in acquiring the field observations. K. Millikan, D. Ortiz-Suslow, M. Fehlberg, and E. Drury provided field assistance. Imperial Beach lifeguards, supervised by Captain R. Stabenow, helped maintain public safety. The YMCA Surf Camp management generously allowed extensive use of their facility for staging and recuperation. The U.S. Navy provided access to Naval property for data collection. M. Okihiro coordinated permits and logistics. R. T. Guza, N. Kumar, M. Spydell, and S. Suanda provided helpful feedback on the manuscript. We thank these people and organizations. Observations and model results used in this work are available through the corresponding author in accordance with AGU data policy. The numerical model, funwaveC, is available at http://iod.ucsd.edu/~falk/funwaveC.html.

References

Brown, J., J. MacMahan, A. Reniers, and E. Thornton (2009), Surf zone diffusivity on a rip-channeled beach, *J. Geophys. Res.*, *114*, C11015, doi:10.1029/2008JC005158.

Brown, J. A., J. H. MacMahan, A. J. H. M. Reniers, and E. B. Thornton (2015), Field observations of surf zone-inner shelf exchange on a rip-channeled beach, *J. Phys. Ocean.*, *45*(9), 2339–2355, doi:10.1175/JPO-D-14-0118.1.

Castelle, B., and G. Coco (2013), Surf zone flushing on embayed beaches, *Geophys. Res. Lett.*, *40*, 2206–2210, doi:10.1002/grl.50485.

Castelle, B., A. Reniers, and J. MacMahan (2014), Bathymetric control of surf zone retention on a rip-channelled beach, *Ocean Dyn.*, *64*(8), 1221–1231.

Chen, Q., J. T. Kirby, R. A. Dalrymple, S. Fengyan, and E. B. Thornton (2003), Boussinesq modeling of longshore currents, *J. Geophys. Res.*, *108*(C11), 3362, doi:10.1029/2002JC001308.

Clark, D. B., F. Feddersen, M. M. Omand, and R. T. Guza (2009), Measuring fluorescent dye in the bubbly and sediment laden surfzone, *Water Air Soil Pollut.*, *204*, 103–115, doi:10.1007/s11270-009-0030-z.

Clark, D. B., F. Feddersen, and R. T. Guza (2010), Cross-shore surfzone tracer dispersion in an alongshore current, *J. Geophys. Res.*, *115*, C10035, doi:10.1029/2009JC005683.

Clark, D. B., F. Feddersen, and R. T. Guza (2011), Modeling surfzone tracer plumes, part 2: Transport and dispersion, *J. Geophys. Res.*, *116*, C11028, doi:10.1029/2011JC007211.

Clark, D. B., S. Elgar, and B. Raubenheimer (2012), Vorticity generation by short-crested wave breaking, *Geophys. Res. Lett.*, *39*, L24604, doi:10.1028/2012GL054034.

Clark, D. B., L. Lenain, F. Feddersen, E. Boss, and R. T. Guza (2014), Aerial imaging of fluorescent dye in the nearshore, *J. Atmos. Oceanic Technol.*, *31*, 1410–1421, doi:10.1175/JTECH-D-13-00230.1.

Feddersen, F. (2007), Breaking wave induced cross-shore tracer dispersion in the surfzone: Model results and scalings, *J. Geophys. Res.*, *112*, C09012, doi:10.1029/2006JC004006.

Feddersen, F. (2012a), Scaling surfzone dissipation, *Geophys. Res. Lett.*, *39*, L18613, doi:10.1029/2012GL052970.

Feddersen, F. (2012b), Observations of the surfzone turbulent dissipation rate, *J. Phys. Ocean.*, *42*, 386–399, doi:10.1175/JPO-D-11-082.1.

Feddersen, F. (2014), The generation of surfzone eddies in a strong alongshore current, *J. Phys. Ocean.*, *44*, 600–617, doi:10.1175/JPO-D-13-051.1.

Feddersen, F., and R. T. Guza (2003), Observations of nearshore circulation: Alongshore uniformity, *J. Geophys. Res.*, *108*(C1), 3006, doi:10.1029/2001JC001293.

Feddersen, F., R. T. Guza, S. Elgar, and T. H. C. Herbers (1998), Alongshore momentum balances in the nearshore, *J. Geophys. Res.*, *103*, 15,667–15,676.

Feddersen, F., D. B. Clark, and R. T. Guza (2011), Boussinesq modeling of surfzone tracer plumes, Part 1: Eulerian wave and current comparisons, *J. Geophys. Res.*, *116*, C11027, doi:10.1029/2011JC007210.

Grant, S. B., J. H. Kim, B. H. Jones, S. A. Jenkins, J. Wasyl, and C. Cudaback (2005), Surf zone entrainment, along-shore transport, and human health implications of pollution from tidal outlets, *J. Geophys. Res.*, *110*, C10025, doi:10.1029/2004JC002401.

Guza, R. T., and F. Feddersen (2012), Effect of wave frequency and directional spread on shoreline runup, *Geophys. Res. Lett.*, *39*, L11607, doi:10.1029/2012GL051959.

Hally-Rosendahl, K., F. Feddersen, and R. T. Guza (2014), Cross-shore tracer exchange between the surfzone and inner-shelf, *J. Geophys. Res. Oceans*, *119*, 4367–4388, doi:10.1002/2013JC009722.

Hally-Rosendahl, K., F. Feddersen, D. B. Clark, and R. T. Guza (2015), Surfzone to inner-shelf exchange estimated from dye tracer balances, *J. Geophys. Res. Oceans*, *120*, 6289–6308, doi:10.1002/2015JC010844.

Harris, T. F. W., J. M. Jordaan, W. R. McMurray, C. J. Verwey, and F. P. Anderson (1963), Mixing in the surf zone, *Int. J. Air Wat. Polut.*, *7*, 649–667.

Inman, D. L., R. J. Tait, and C. E. Nordstrom (1971), Mixing in the surfzone, *J. Geophys. Res.*, *26*, 3493–3514.

Kennedy, A. B., Q. H. Chen, J. T. Kirby, and R. A. Dalrymple (2000), Boussinesq modeling of wave transformation, breaking and runup I: One dimension, *J. Waterw. Port Coastal Ocean Eng.*, *126*, 39–47.

Lentz, S. J., M. Fewings, P. Howd, J. Fredericks, and K. Hathaway (2008), Observations and a model of undertow over the inner continental shelf, *J. Phys. Oceanogr.*, *38*(11), 2341–2357, doi:10.1175/2008JPO3986.1.

Lynett, P. (2006), Nearshore modeling using high-order Boussinesq equations, *J. Waterw. Port Coastal Ocean Eng.*, *132*, 348–357.

MacMahan, J., et al. (2010), Mean Lagrangian flow behavior on an open coast rip-channeled beach: A new perspective, *Mar. Geol.*, *268*(14), 1–15, doi:10.1016/j.margeo.2009.09.011.

Nwogu, O. (1993), Alternative form of Boussinesq equations for nearshore wave propagation, *J. Waterw, Port Coastal Ocean Eng.*, *119*, 618–638.

Peregrine, D. H. (1998), Surf zone currents, *Theor. Comput. Fluid Dyn.*, *10*, 295–309.

Rippy, M. A., P. J. S. Franks, F. Feddersen, R. T. Guza, and J. A. Warrick (2013), Beach nourishment impacts on bacteriological water quality and phytoplankton bloom dynamics, *Environ. Sci. Technol.*, *47*, 6146–6154, doi:10.1021/es400572k.

Salmon, R. (2002), Numerical solution of the two-layer shallow water equations with bottom topography, *J. Mar. Res.*, *60*, 605–638.

Sinnett, G., and F. Feddersen (2014), The surf zone heat budget: The effect of wave heating, *Geophys. Res. Lett.*, *41*, 7217–7226, doi:10.1002/2014GL061398.

Spydell, M., F. Feddersen, R. T. Guza, and W. E. Schmidt (2007), Observing surfzone dispersion with drifters, *J. Phys. Oceanogr.*, *27*, 2920–2939.

Spydell, M. S., and F. Feddersen (2009), Lagrangian drifter dispersion in the surf zone: Directionally spread, normally incident waves, *J. Phys. Oceanogr.*, *39*, 809–830.

Spydell, M. S., F. Feddersen, and R. T. Guza (2009), Observations of drifter dispersion in the surfzone: The effect of sheared alongshore currents, *J. Geophys. Res.*, *114*, C07028, doi:10.1029/2009JC005328.

Spydell, M. S., F. Feddersen, J. H. MacMahan, and R. T. Guza (2014), Relating Lagrangian and Eulerian horizontal eddy statistics in the surf zone, *J. Geophys. Res. Oceans*, *119*, 1022–1037, doi:10.1002/2013JC009415.

Spydell, M. S., F. Feddersen, M. Olabarrieta, J. Chen, R. T. Guza, B. Raubenheimer, and S. Elgar (2015), Observed and modeled drifters at a tidal inlet, *J. Geophys. Res. Oceans*, *120*, 4825–4844, doi:10.1002/2014JC010541.

Suanda, S. H., and F. Feddersen (2015), A self-similar scaling for cross-shelf exchange driven by transient rip currents, *Geophys. Res. Lett.*, *42*, 5427–5434, doi:10.1002/2015GL063944.

Suanda, S. H., J. A. Barth, R. A. Holman, and J. Stanley (2014), Shore-based video observations of nonlinear internal waves across the inner shelf, *J. Atmos. Oceanic Technol.*, *31*(3), 714–728, doi:10.1175/JTECH-D-13-00098.1.

Suanda, S. H., S. Perez, and F. Feddersen (2016), Evaluation of a source-function wavemaker to accurately generate random directionally spread waves, *Coastal Eng.*, in press.

Tennekes, H., and J. L. Lumley (1972), *A First Course in Turbulence*, MIT Press, Cambridge, Mass.

Tulloch, R., R. Ferrari, O. Jahn, A. Klocker, J. LaCasce, J. R. Ledwell, J. Marshall, M.-J. Messias, K. Speer, and A. Watson (2014), Direct estimate of lateral eddy diffusivity upstream of drake passage, *J. Phys. Oceanogr.*, *44*(10), 2593–2616, doi:10.1175/JPO-D-13-0120.1.

Walter, R. K., C. B. Woodson, P. R. Leary, and S. G. Monismith (2014), Connecting wind-driven upwelling and offshore stratification to nearshore internal bores and oxygen variability, *J. Geophys. Res. Oceans*, *119*, 3517–3534, doi:10.1002/2014JC009998.

Wei, G., J. T. Kirby, and A. Sinha (1999), Generation of waves in Boussinesq models using a source function method, *Coastal Eng.*, *36*, 271–299.